Mechanical instability of electrode-electrolyte interfaces in solid-state batteries

Giovanna Bucci,[1,2,*] Brandon Talamini,[3,†] Ananya Renuka Balakrishna,[1] Yet-Ming Chiang,[1] and W. Craig Carter[1]

[1]*Massachusetts Institute of Technology, Department of Materials Science and Engineering,*
77 Massachusetts Avenue, Cambridge, Massachusetts 02139-4307, USA

[2]*Robert Bosch LLC, Research and Technology Center, Sunnyvale, California 94085, USA*

[3]*Massachusetts Institute of Technology, Department of Mechanical Engineering,*
77 Massachusetts Avenue, Cambridge, Massachusetts 02139-4307, USA

The interfacial contact between active material and solid electrolyte in a composite electrode limits the kinetics of all-solid-state batteries (ASSB). Despite the progress in processing techniques to improve cohesion in composite electrodes, the electrochemical reactions and mechanical stresses developed during battery operation affects interface properties. Here, we propose a one-dimensional radially symmetric analytical model based on the cohesive theory of fracture, to investigate the mechanical stability of interfaces in ASSB microstructures. Using the cohesive-energy approach, we analyze the delamination criterion and derive a stability condition for fracture propagation. Furthermore, we investigate the role of particle size and material properties on delamination, and we explore the effect of delamination on area-specific impedance. We report that delamination is induced when electrode particles undergo a volumetric change of about 7.5% during (de)intercalation. Compliant electrolytes ($E < 25$ GPa) are found to accommodate up to 25% of particle volume change and delay the onset of delamination. The study identifies geometric regimes for mechanical stability. Such regimes are based on the relative size of the damage zone with respect to the particle radius. Finally, we demonstrate that delamination can significantly influence the total charge/discharge time if highly conductive electrolytes are employed. Overall, the analyses provide guidelines for engineering electrode-electrolyte interfacial properties by controlling particle size, material stiffness, and adhesive strength and length scale.

I. INTRODUCTION

All-solid-state batteries (ASSBs) are being pursued as potentially safe high-energy storage systems [1–4]. The replacement of an organic liquid electrolyte with a nonflammable inorganic solid electrolyte (SE) improves Li-ion battery (LIB) safety. Despite the progress in achieving high bulk conductivity, the rate capability of most all-solid-state cells remains poor [1,5,6]. This is typically ascribed to high resistance at the interfaces, but the exact mechanisms have been difficult to ascertain experimentally [7–10]. Chemical incompatibility, electrochemical reactions, and mechanical damage may all contribute to degrading interfacial kinetics and battery performance. Fracture in solid Li-ion conductors creates a barrier for Li transport, therefore mechanical degradation is linked to the battery power density. One design strategy for making solid-state electrodes is to fill a scaffold of SE with active particles [11]. This configurations accommodates intercalation-induced deformations but lowers the contact area between the electrolyte and the active material. Another strategy is to create low porosity composites via pressing or sintering. These systems have lower internal resistance but they are more prone to mechanical degradation.

Bulk-type ASSBs have composite electrodes made of particles of active material (AM), embedded in a matrix of solid electrolyte and electronic conductive carbon. Several processing methods have been developed in order to improve internal cohesion of the electrode's microstructure [12–20]. However, electrode-electrolyte interfaces may delaminate *in operando*.

Electrode particles made of polycrystalline intercalation compounds are subject to chemical expansion (i.e., change in volume caused by compositional change). The cyclic expansion and contraction of electrode particles in charge-discharge cycles can eventually lead to de-bonding from the conducting SE-carbon matrix. In particular, positive electrodes are typically assembled in the lithiated state and tend to decrease volume upon delithiation [21,22]. Cell impedance growth follows from an incomplete (or imperfect) contact between particles and the SE matrix. Capacity fade will also occur if particles of the active material become completely isolated. Here we investigate the mechanical reliability of interfaces in ASSB microstructures. The mechanical response is characterized by delamination and, in some cases, by a nonequilibrium transition from a coherent to a fully debonded interface. We will show that, for some combinations of material properties, "brittle" delamination occurs. For other combinations a "ductile" delamination occurs where the interface fails in a continuous fashion. More complex phenomena may arise where delamination may not be the prevailing fracture mode. For example, competing mechanisms of crack formation in

---

the bulk electrode or electrolyte material, or the formation of new phases at the interface from the decomposition of the solid electrolyte at high voltages [23–25], may arise. These different scenarios will be investigated in future studies.

In this paper, we formulate an analytical model to investigate the effects of electrode particle size and adhesion on the mechanical stability of interfaces in ASSB microstructures. The one-dimensional radially symmetric analytic model is based on Del Piero's analysis of cohesive theory of fracture [26]. Hypotheses of the analysis are a sharply defined interface and the condition that the interfacial toughness is less than the toughness of either of the two adjoining materials. We consider the volume change associated with changes in Li content as the loading condition for fracture nucleation and propagation. According to our analysis, most intercalating compounds undergo enough chemical strain to suffer from mechanical degradation. Once nucleated, fracture may propagate gradually ("ductile") or suddenly ("brittle"). A smooth gradual opening of the crack is preferable. The relative stiffness of the interface with respect to the SE material contributes to the stability of fracture. The derived stability ranges can be used to design the microstructure of a composite positive electrode resistant to sudden mechanical degradation. Our analyses provide guidelines for the engineering of particle size, volume ratio of active material, and interfacial properties.

Several studies of interfacial delamination can be found in the fracture mechanics literature [27–29]. For instance, the phenomenon of spontaneous delamination of coatings under residual stress from a substrate has been extensively treated.[1] Pioneering studies in the field of interfacial delamination [27,30–32] have indicated that a key parameter controlling the overall stress to strain response is the ratio between two length scales: the structure size (characteristic of the problem) and the cohesive length (constitutive behavior of the interface). Large values of the structure vs the cohesive length lead to brittle delamination. In agreement with these studies [27,30–32], we demonstrate that a wider stability range can be achieved with nanostructured electrodes, where the particles and their spacing have size of the order of 100 nm. Alternatively, the interface can be engineered to achieve larger cohesive length (i.e., by allowing forces to be transmitted across the interface for wider openings of the crack). For example, rough interfaces will have a larger cohesive length scale.

While reducing the particle size improves the stability of crack growth, it does not prevent fracture. Our analysis shows that the condition for crack nucleation is independent of the particle size. However, ductility of solid electrolyte materials improves mechanical reliability. Plastic flow of the electrolyte to accommodate the particle's volume change would preserve the interface from debonding. Perhaps the mechanical properties of ceramics and polymer solid electrolytes can be engineered to make them ductile.

Bulk and interface constitutive behaviors are assumed to be rate independent, therefore the solution does not depend on the battery charging rate.

II. ANALYSIS OF THE DELAMINATION AT THE ELECTRODE-ELECTROLYTE INTERFACE VIA A COHESIVE-ZONE MODEL

We model an elementary unit of the microstructure that comprises a spherical electrode-particle embedded in a solid-electrolyte shell (see Fig. 1). We assume that this region is unaffected by nearby particles. Furthermore, we assume the chemical expansion of the electrolyte material to be isotropic and a linear function of the Li content. These approximations reduce the problem to a radially symmetric one-dimensional (1D) analysis (see Fig 2).

The electrode particle radius evolves from its initial strain-free state R_A as a function of the battery state of charge c. The size change of the electrode particle drives mechanical loading of the interface and the surrounding electrolyte. This interaction is represented with a cohesive model. Our analytical model includes the electrolyte shell and the cohesive interface (see Fig. 2). The electrode particle is not modeled explicitly, and its radius change is represented by the boundary displacement $\underline{u}(c)$ applied to the inner part of the cohesive interface. The electrode particle radius change is proportional to the Vegard's parameter α, representing the lattice strain associated with the accommodation of lithium. The total displacement imposed on the inner cohesive interface is thus $\underline{u}(c) = \alpha c R_A$. The problem reduces to a displacement-controlled fracture test in one spatial dimension.

At each loading step, a displacement $u(R)$ is associated with the radial coordinate $R \in [R_A, R_B]$, R_A and R_B being the internal and external radii of the electrolyte shell (see Fig. 1). The opening of the interface is characterized by the displacement jump $[\![u]\!]$, i.e., a discontinuity in the displacement function $u(R)$ at $R = R_A$. By compatibility, the total applied displacement $\underline{u}$ decomposes into the stretching of the electrolyte and the irreversible opening of the interface $[\![u]\!]$. Before fracture nucleates, $[\![u]\!] = 0$ and the electrolyte deformation is function of the particle's state of charge. The boundary conditions on the displacement field are

$$u(R_B) = 0 \quad u(R_A) = \alpha c R_A. \tag{1}$$

The general linear elastic solution for the equilibrium of a hollow, spherical solid subjected to spherically symmetric boundary conditions is

$$u(R) = C_1 R + \frac{c_2}{R^2}. \tag{2}$$

With the boundary conditions of Eq. (1), the displacement field in the electrolyte reads

$$u(R) = \frac{R_A^3 \alpha c}{R_A^3 - R_B^3} \left(R - \frac{R_B^3}{R^2} \right). \tag{3}$$

In our treatment, the external radius R_B is a function of the particle size, by means of a scaling factor f. This scaling factor is in turn a function of the volume ratio of active

---

[1]We clarify that the form of instability discussed here is a different phenomena than buckling of thin film layer coatings, as the two adjoining materials have comparable thicknesses.
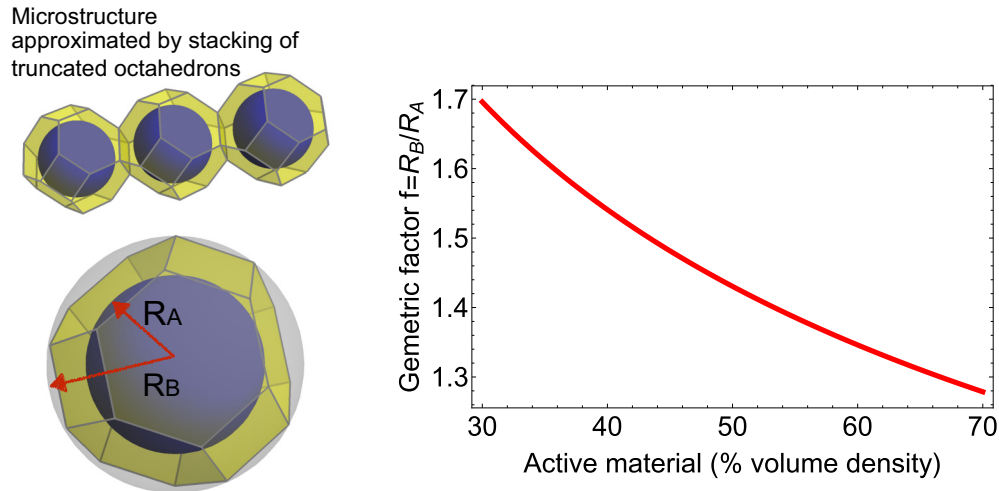
FIG. 1. The electrode microstructure is idealized by an assembly of space-filling truncated octahedra. Each polyhedron embeds an electrode particle and it is treated as a representative volume. The external surface of the electrolyte shell is close to spherical, therefore we assume radial symmetry. The thickness of the electrolyte shell, with respect to the particle radius, depends on the volume ratio occupied by the particles. Typical values of active material loading are in the range 50–60% for commercial batteries. On the right the geometric factor $f = R_B/R_A$ is plotted as a function of active material loading.

material ϕ_{AM} (i.e., volume of the electrode particles vs the total volume of the electrode). Based on the geometric construction illustrated in Fig. 1, the function $f(\phi_{AM})$ is easily derived (right plot in Fig. 1).

Substituting $R_B = f R_A$, we rewrite Eq. (3) as

$$u(R) = \frac{\alpha c \left(R_A^3 f^3 - R^3 \right)}{(f^3 - 1) R^2}. \tag{4}$$
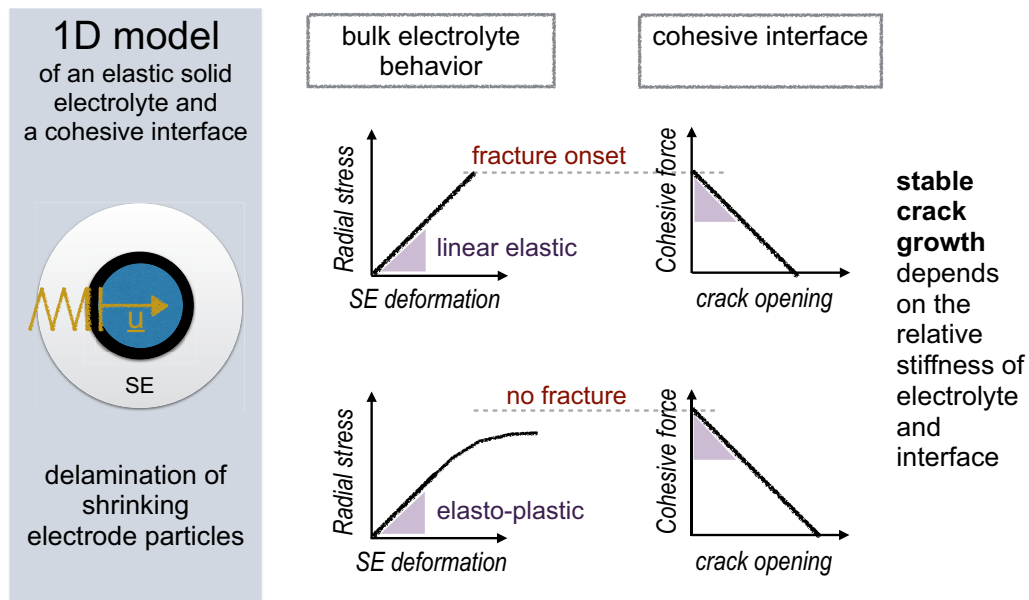

FIG. 2. Schematic representation of the 1D analysis carried out. A single particle is idealized as spherical in shape and it is embedded in a shell of solid electrolyte. The solid electrolyte material is visualized by an elastic spring and the interface by a cohesive traction-separation law. The spring is a schematic for illustrative purposes; the model is a continuum solid. The particle changes its volume following the change in stoichiometry. During battery charge Li deintercalates from the positive electrode causing, in most cases, the active material to contract. We do not model the individual electrode particles explicitly, but we regard their radius change as an imposed displacement $\underline{u}$. Constitutive laws for the solid electrolyte and the cohesive interface are sketched. The SE layer linear elastic response consists of a monotonic function of its total elongation (stretching of the spring). The interface is modeled with a linear traction separation law. The traction transmitted across the interface is a decreasing function of the displacement jump, i.e., the separation of the interface. The interface becomes fully debonded when a critical opening is reached and the cohesive force is null. If the solid-electrolyte material is elastoplastic, the emergence of plastic flow in proximity of the interface may bound the stress and prevent delamination to occur. The object of this study is the classification of regimes of no-fracture, stable crack growth and of sudden mechanical failure of the electrode-electrolyte interface.

From the displacement function, the radial and hoop strain fields can be calculated as $\epsilon_{RR} = \partial u / \partial R$ and $\epsilon_{\theta\theta} = u/R$. The radial and hoop stresses are the following:

$$\sigma_{RR}(R) = \frac{\lambda}{\nu}[(1-\nu)\epsilon_{RR} + 2\nu\epsilon_{\theta\theta}]$$

$$= \frac{\alpha c \lambda [2R_A^3 f^3(2\nu-1) - (\nu+1)R^3]}{(f^3-1)\nu R^3} \quad (5)$$

$$\sigma_{\theta\theta}(R) = \frac{\lambda}{\nu}(\nu\epsilon_{RR} + \epsilon_{\theta\theta})$$

$$= -\frac{\alpha c \lambda [R_A^3 f^3(2\nu-1) + (\nu+1)R^3]}{(f^3-1)\nu R^3}. \quad (6)$$

In the expressions above, λ and ν are two elastic properties of the electrolyte material. In particular λ is the first Lamé constant and ν is Poisson's ratio.[2]

In the next paragraph we analyze the conditions for delamination to occur. Subsequently, we derive a stability condition for fracture propagation.

Criterion for delamination. Cohesive energy models are based on the idea that the fracture energy, instead of being released instantaneously at crack initiation as in Griffith's model, is released gradually with the growth of the crack opening. The gradual release presumes some cohesion between the separating flanks of a crack. Generally, the traction decays with increasing separation, until it vanishes at a critical opening displacement that is an intrinsic characteristic of the given interface. The critical opening displacement introduces an intrinsic length scale and embeds a size effect into the fracture problem [33]. Cohesive models have been used extensively since Barenblatt and Dugdale first proposed them. However, their mathematical character has been analyzed only recently by Del Piero [26]. The discussion on fracture instability presented here follows the lines of Del Piero's work.

The total energy of the system includes the elastic energy, as a bulk volumetric term, and a cohesive energy per unit area. For the 1D model discussed here, the total energy per unit of the particle's surface area can be written as follows:

$$E(u, [\![u]\!]) = \int_{R_A}^{R_B} k_{el}(u'(R))^2 dR + G([\![u]\!]). \quad (7)$$

The first term in Eq. (7) represents the elastic energy stored in the electrolyte shell and it depends on its stiffness k_{el} and on the radial strain $u'(R)$. The second term represents the cohesive energy. For instance the quadratic form

$$G([\![u]\!]) = F_c\left([\![u]\!] - \frac{F_c}{4\gamma_{am-se}}([\![u]\!])^2\right), \quad (8)$$

has two fundamental parameters: the interfacial energy release rate $\gamma_{am-se} = \lim_{[\![u]\!] \to [\![u]\!]_R} G([\![u]\!])$ (where $[\![u]\!]_R$ is the critical opening displacement) and the adhesive strength F_c. The adhesive strength may be calculated from first principles [34–36]. The form of $G([\![u]\!])$ in Eq. (8) is associated with

a linear traction-separation law $G'([\![u]\!])$, like the one represented in Fig. 2. In monotonic quasistatic loading conditions, the solid-electrolyte shell is stretched, until a critical opening displacement $[\![u]\!]_R$ is reached:

$$G'([\![u]\!]_R) = F_c\left(1 - \frac{F_c}{2\gamma_{am-se}}([\![u]\!]_R)\right) = 0,$$

$$[\![u]\!]_R = \frac{2\gamma_{am-se}}{F_c}. \quad (9)$$

Fracture nucleation occurs when the stress at the electrode-electrolyte interface reaches the value of the adhesive strength F_c. The criterion $\sigma_{RR}(A) = F_c$ can be used to identify the state of charge at which delamination occurs. From Eq. (5), the intercalation induced strain sufficient to cause delamination can be calculated as follows:

$$(\alpha c)_{\text{fracture}} = -\frac{F_c(f^3-1)\nu}{\lambda[f^3(4\nu-2) - \nu - 1]}. \quad (10)$$

According to Eq. (10), the SE elastic properties, the interfacial cohesive strength, and the active material loading contribute to the critical relative displacement of the interface. To generalize the discussion to various intercalating compounds, we focus on the total anelastic deformation $(\alpha c)_{\text{fracture}}$. This strain can be achieved at various states of charge, depending on Vegard's parameter for the specific material.

The contour regions in Fig. 3(a) represent the ranges of relative volume contraction of the electrode particle as a function of the E_{se} (electrolyte's Young's modulus) and γ_{am-se} (interface fracture energy). For most combinations of (E_{se}, γ_{am-se}) values, delamination initiates when particles have changed their radius by only 2.5% (and their volume by about 7.5%), a value that encompasses the behavior of many intercalation compounds [21,22]. Only in the case of very compliant electrolytes, with $E_{se} < 25$ GPa and large interfacial cohesive energy ($\gamma_{am-se} > 5$ Jm^{-2}), are chemical strains greater than 25% required. In addition to interfacial engineering, the bulk elastic properties of the electrolyte provide a way to control microstructure reliability. Compliant electrolytes are preferable to maintain interfacial cohesion.

The contour plot of Fig. 3(a) is representative of the case with cohesive length $[\![u]\!]_R = 1$ nm. An even smaller deformation is needed to initiate fracture at interfaces with larger cohesive length. In Fig. 3(a), the interfacial fracture energy γ_{am-se} illustrated is in the range of 1–10 J/m^2. With $[\![u]\!]_R = 1$ nm, it follows that the adhesive traction F_c range is 2–20 GPa.

In Fig. 3(a), we consider solid electrolytes with modulus between 20 and 200 GPa [37]. The interfacial cohesive strength is expected to be smaller than the bulk value and strongly dependent on the electrode manufacturing. Figure 3(b) shows a linear dependence between the intercalation induced strain and the bulk stiffness of the electrolyte. For a given fracture energy, the cohesive strength F_c decreases with the cohesive length $[\![u]\!]_R$. The same dependencies occur for different cohesive lengths as illustrated in Fig. 3(a).

This analysis leads to the conclusion that particle delamination is a likely event in solid-state-electrode microstructures. Furthermore, fracture cannot be alleviated by simply choosing a smaller particle size.

---

[2]The equations above can be written in terms of the Young's modulus E and Poisson's ratio ν, by substituting $\lambda = E\nu/(1-2\nu)(\nu+1)$.
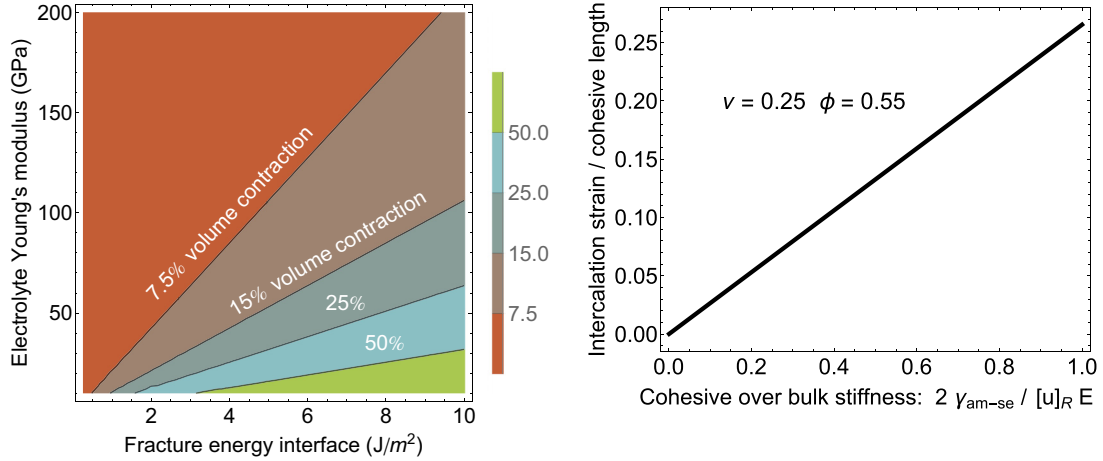
FIG. 3. (a) The contour plot on the left shows the relative volume contraction of electrode particles [according to Eq. (10)]. For most combinations of material properties, interfacial fracture energy, and electrolyte stiffness, 2.5% of radial strain (corresponding 7.5% volume change) is sufficient to nucleate fracture. Such a low Vegard's strain is typical for most Li-intercalating compounds. Compliant solid electrolyte materials are preferable to avoid delamination. Cohesive length is fixed at 1 nm. (b) The chemical strain required to fracture decreases with the length of the fracture process zone. The plot shows a generalization of the result in (a) illustrated in nondimensional form. The intercalation strain is normalized with respect to the interfacial cohesive length. The horizontal axis represents the ratio between cohesive stiffness (i.e., the slope of the traction separation law in Fig. 2) and the electrolyte Young's modulus. The cohesive stiffness is negative; here we consider the absolute value $2\gamma_{am-se}/[[u]]_R$.

Stability of fracture. After fracture initiates, the system evolves with increasing opening of the interface and progressive unloading of the electrolyte. The total displacement $u + [[u]] = \alpha c R_A$ is constrained by the compatibility with the particle's radius change. The partitioning of the total displacement into the bulk and interfacial components (u and $[[u]]$ respectively) depends on the relative stiffness of the elastic material and of the interface.

A complete unloading of the SE ($u(R) = 0, R \in [R_A, R_B]$) may be attained before a crack opening is complete ($[[u]] < [[u]]_R$). In this case, a sharp nonequilibrium transition leads to the totally fractured configuration. Stable conditions, instead, promote a gradual opening of the interface.

We seek to identify the regime of stability for the crack opening at the electrode-electrolyte interface in quasistatic conditions. After fracture nucleates, the boundary conditions (BCs) at the interface change. The radially symmetric displacement evolving with the state of charge is replaced by a mixed condition on both displacement and traction. Such mixed Robin BCs simultaneously impose force balance and compatibility with the particle's radius change.

In order to guarantee equilibrium of forces, the radial stress needs to evolve to balance the cohesive traction, so the condition $\sigma_{RR} = F_c$ is enforced throughout the process. Upon monotonic loading the cohesive force decays with the opening of the interface, while the solid electrolyte shell undergoes elastic unloading. It follows that the average radial strain in the electrolyte decreases with the opening of the crack. The equilibrium states for a representative system are drawn in red in the $u(A)$ vs $[[u]]$ plane; see Fig. 4. The vertical branch of the red curve corresponds to a nonfractured state with $[[u]] = 0$. The kinking point represents the critical displacement at the onset of fracture. The slope of the descending curve is uniquely defined by the partitioning of the total applied displacement into bulk and interfacial terms. In other

words, the slope depends on the relative (negative) stiffness of the interface and the bulk stiffness of the electrolyte material.

In addition to the equilibrium condition, the displacements $u(R_A)$ and $[[u]]$ are constrained by the compatibility with the external load. At each state of charge, solutions to the equation $u(R_A) + [[u]] = \alpha c R_A$ define a line in the $u(R_A)$ vs $[[u]]$ plane. The black lines in Fig. 4 are drawn for increasing values of the total displacement (or increasing state of charge). The mixed boundary condition described earlier implies that both equilibrium and compatibility are satisfied at the particle-electrolyte interface. This can be visualized as finding the intersection between the red equilibrium curve and the black compatible loading curves in Fig. 4. Such intersections can be found at every stage of delamination only if the slope of the black curves is lower than the equilibrium curve, as illustrated in Fig. 4(b). Conversely, in Fig. 4(a) the loading lines do not intersect the equilibrium curve beyond the kinking point [corresponding to $u = (\alpha c)_{\text{fracture}}$], because they have a larger slope. In this case, the interface is expected to undergo a sudden transition from a fully coherent to a fully noncoherent state.

Because we assumed a linear elastic behavior for the SE material and a linear traction-separation law, the equilibrium curve is linear. More general forms of bulk and cohesive energies can be considered, leading to a nonlinear equilibrium condition between bulk and interfacial displacement. For equilibrium curves with nonconstant derivative the point of instability does not necessarily coincide with the onset of fracture. In the case of partially stable interfaces, the cohesive energy is released instantaneously once the unstable point is reached.

We calculate the critical particle radius A_{critical} that defines the transition from stable to unstable crack growth. The critical particle size can be derived by constraining the slope of the compatibility curve to be lower than the slope of the
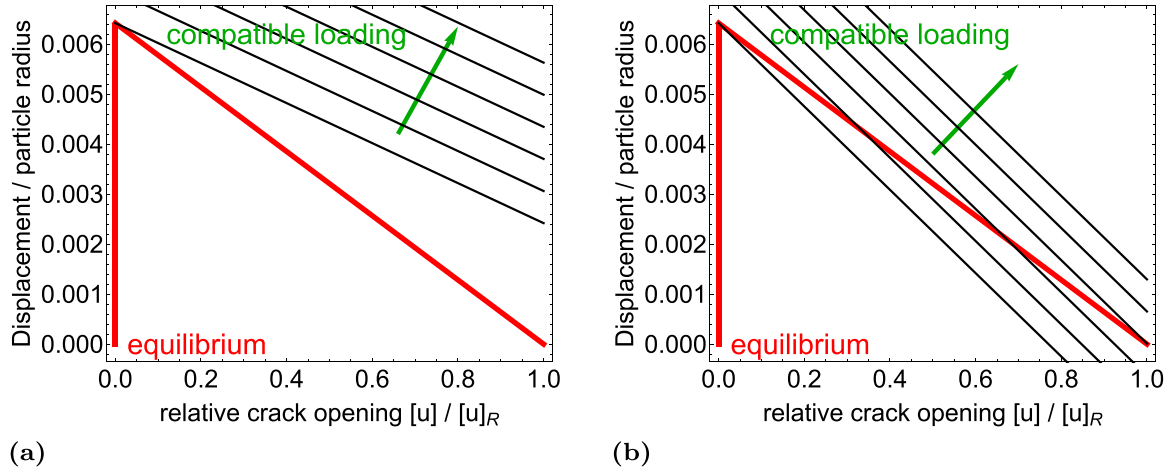
FIG. 4. The two plots illustrate the difference between mechanically (a) unstable and (b) stable interfaces in the plane defined by the relative crack opening and the relative displacement of the interface. The red curves represent the equilibrium configurations obtained by imposing the balance between the radial force in the electrolyte shell and the cohesive force at the interface. Before fracture occurs, the opening of the interface is zero and the first part of the equilibrium curve is vertical. After nucleation, the slope of the red curve depends on the relative stiffness of bulk SE material and interface according to the equation $u/R_A = -(1/A_{critical})(\llbracket u \rrbracket / \llbracket u \rrbracket_R)$ and the definition of $A_{critical}$ as in Eq. (11). The black lines are constructed by imposing the compatibility with the external loading (i.e., the displacement due to the shrinking particle). The black line shifts up as the particle continues shrinking according to equation $\llbracket u \rrbracket / \llbracket u \rrbracket_R = \alpha c - u/R_A$ for increasing values of $\alpha c \geqslant (\alpha c)_{fracture}$. In (a) there is no intersection between compatible and equilibrium curves after fracture nucleates. This is interpreted as a nonsmooth transition from a fully coherent to a fully incoherent electrode-electrolyte interface.

equilibrium curve. This is equivalent to finding a minimizer for the energy function in Eq. (7):

$$A_{critical} = \frac{\lambda(f^3(2+4\nu)+\nu+1)}{(f^3-1)\nu} \frac{\llbracket u \rrbracket_R}{F_c}$$

$$= \frac{E(f^3(2+4\nu)+\nu+1)}{(f^3-1)(1-2\nu)(\nu+1)} \frac{\llbracket u \rrbracket_R}{F_c}. \quad (11)$$

Rewriting the expression above in nondimensional form, we obtain

$$\frac{A_{critical}}{\llbracket u \rrbracket_R} = \frac{E}{F_c} \frac{f^3(2-4\nu)+\nu+1}{(f^3-1)(1-2\nu)(\nu+1)}. \quad (12)$$

The left-hand side in Eq. (12) is the critical particle's radius (length scale of the microstructure) normalized with respect to the critical opening displacement (length scale of the crack process zone). On the right-hand side the factor E/F_c is the ratio between the electrolyte Young's modulus and the cohesive strength; the second factor is a function of the SE Poisson's ratio and volume fraction.

We illustrate the dependence of the normalized critical particle size $A_{critical}/\llbracket u \rrbracket_R$ on the other dimensionless variables appearing in Eq. (12). Fig. 5 shows a weak dependence of the stable particle size on the active material loading and on the SE Poisson's ratio (up to 0.3). The result mainly depends on the electrolyte's stiffness and the cohesive strength. The cohesive length is typically of the order of 1 nm, therefore we predict the particle radius to be bounded in the range 50–500 nm.

The size of the crack process zone is defined by the interfacial opening $\llbracket u \rrbracket_R$ at the completion of fracture. This length scale identifies a region ahead of the crack tip where delamination is in progress. Stability is promoted in presence of a large cohesive length scale (i.e., by allowing forces to

be transmitted across the interface for wider openings of the crack). Nanoscale electrode particles favor stable crack growth, but they do not prevent the crack nucleation. The onset of delamination is independent of the particle size.

Stable configurations are also characterized by large SE stiffness and low interfacial fracture strength F_c. These requirements contrast with the conditions for crack nucleation: First, a complaint electrolyte (small stiffness) is better for preventing or delaying crack formation. Second, Eq. (10) suggests a high interfacial fracture strength F_c is needed to avoid crack nucleation. However, once a crack nucleates in a compliant electrolyte, its propagation is prone to be unstable; see Eqs. (11) and (12). A much wider range of materials [corresponding to (E, F_c) pairs] can be used, in combination with nanostructured electrodes.

Designing densely packed solid-state-electrode microstructures is desirable for achieving high-energy density and also to favor stable interfaces. Limitations on accessible capacity are imposed by inadequate ion transport through a diminishing volume of tortuous, electrolyte-filled pores.

In the analyses presented here, the fracture energy of the interface is treated as a constant. However, this property will generally depend on the lithium content and therefore vary with the state of charge. If the fracture energy increases with Li content, the positive electrode will gain mechanical stability as the battery is being charged. The opposite trend is to be expected if the presence of Li reduces the toughness of the interface. That is, if lithium acts as a surfactant.

Also, the result in Eq. (12) can be generalized to include more complex constitutive behaviors for bulk and interface.

Exploit electrolyte ductility to prevent delamination. In addition to a linear elastic behavior considered so far, we admit the possibility for the solid electrolyte material to deform plastically. We want to identify cases where the yielding
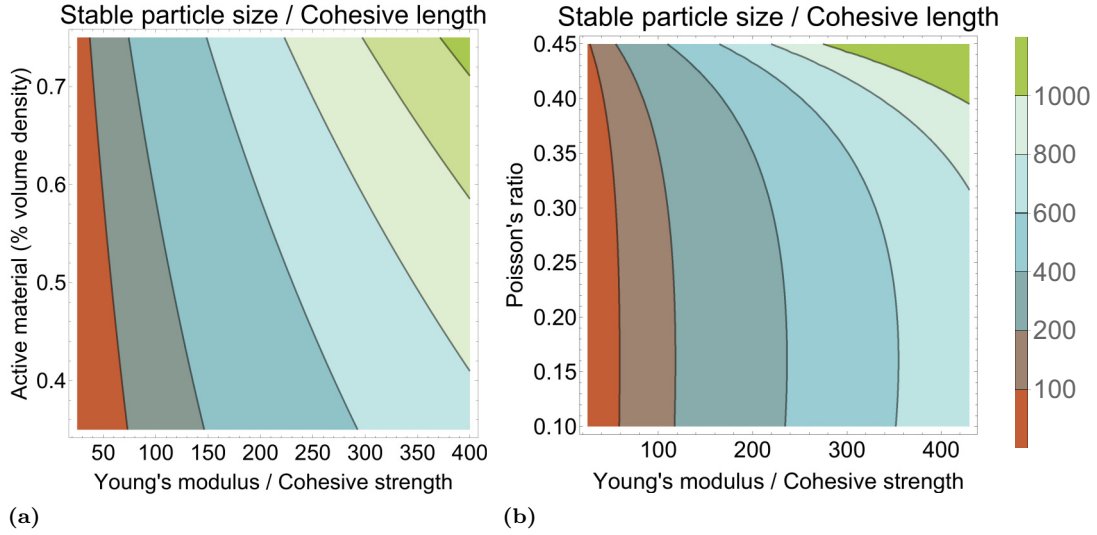
FIG. 5. Regimes of stable vs unstable delamination at the electrode particle interface are represented. According to Eq. (12), fracture stability depends on three dimensionless parameters. The parameter on the horizontal axis is descriptive of the constitutive behavior of the SE material (Young's modulus E_{se}) and of the interface (cohesive strength F_c). The particle's radius A and cohesive length $[\![u]\!]_R$ are the governing length scales for this problem. The contour lines define the stable particle size normalized by the cohesive length. Mechanical stability can also be achieved by increasing the cohesive length or decreasing the particle size. For a fixed volume ratio of active material, stability improves with the stiffness of the solid electrolyte. The dependence on the Poisson's ratio is weak, unless the SE material is close to being incompressible.

condition is met before the onset of fracture. If the solid electrolyte material is able to deform plastically, the development of dislocations would relax the stress and prevent it from overcoming the interfacial cohesive strength.

Both the von Mises and Tresca criteria[3] for the spherically symmetric problem reduce to $\sigma_{\theta\theta} - \sigma_{RR} = \sigma_{\text{yield}}$. Plasticity occurs at first on the internal boundary of the electrolyte shell (at $x = R_A$), it propagates through the electrolyte material, and eventually reaches the external interface ($x = R_B$). Two examples of radial, hoop, and von Mises stress fields are plotted in Fig. 6. As the particle shrinks, the solid electrolyte is stretched in the radial direction and, therefore, is under tension. In the case of Poisson's ratio $\nu = 0.15$ illustrated in Fig. 6(a), the hoop stress is compressive at the interface and it changes sign through the solid-electrolyte thickness. The assumptions for the other parameters are indicated in the figure. The von Mises stress is negative, indicating that the condition for yielding may be reached in compression.

The Vegard's strain necessary to cause the electrolyte to undergo plastic flow at the electrode-electrolyte interface is

$$(\alpha c)_{\text{plastic}} = -\frac{(f^3 - 1)\nu\sigma_{\text{yield}}}{3 f^3 \lambda (2\nu - 1)}. \tag{13}$$

Assuming that σ_{yield} is constant (i.e., the electrolyte material does not harden) we compare Eqs. (13) and (10) to impose the condition $|(\alpha c)_{\text{plastic}}| < |(\alpha c)_{\text{fracture}}|$. The inequality

$$\frac{(\sigma_{\text{yield}}/F_c)(f^3(2 - 4\nu) + \nu + 1)}{3 f^3 (1 - 2\nu)} < 1 \tag{14}$$

---

[3]The von Mises and Tresca criteria are based on comparing an equivalent scalar value of stress, which can be computed from the Cauchy stress tensor, to the material yield strength.

defines the cases where plastic flow of SE material at the interface prevents delamination. Equation (14) does not depend on the particle size or the electrolyte's stiffness. However, it depends strongly on the interfacial cohesive strength, on the SE Poisson's ratio ν, and the yield stress. Note that the yield stress is sensitive to the presence of defects and material processing, which are not considered in Eq. (14). A weak dependence on the active material loading is also observed.

We illustrate the competition between plasticity and delamination in the parameter space defined by $\sigma_{\text{yield}}/F_c$ and ν (see Fig. 7). The grey region on the left of the contour lines identifies the conditions for plastic flow. A brittle behavior should be expected, if the system falls in the white region on the right of Fig. 7. The four contour lines correspond to four different values of active material loading, $\phi_{AM} = 0.4$, 0.5, 0.6, 0.7, in order from right to left.

From Fig. 7, it is apparent that delamination is prevented in any case of practical interest under the condition $\sigma_{\text{yield}} < 0.5 F_c$. Solid electrolyte materials that have enough ductility to accommodate intercalation-induced strains are certainly preferable for bulk-type batteries. Given typical battery charge/discharge times, we expect the strain rate imposed on the electrolyte to allow for plastic flow.

A. Effect of electrode particles' delamination on area-specific impedance

Delamination of electrode particles is expected to increase the time required for lithium to intercalate or deintercalate the particle. Interfacial fracture reduces the contact area with the Li-ion conducting phase, thus decreasing the average diffusivity of Li across the electrode. Here we estimate the reduced transport properties by a random walk analysis. The change of first passage times (FPTs) with increasing delamination is indicative of the effective total interfacial resistance. We treat
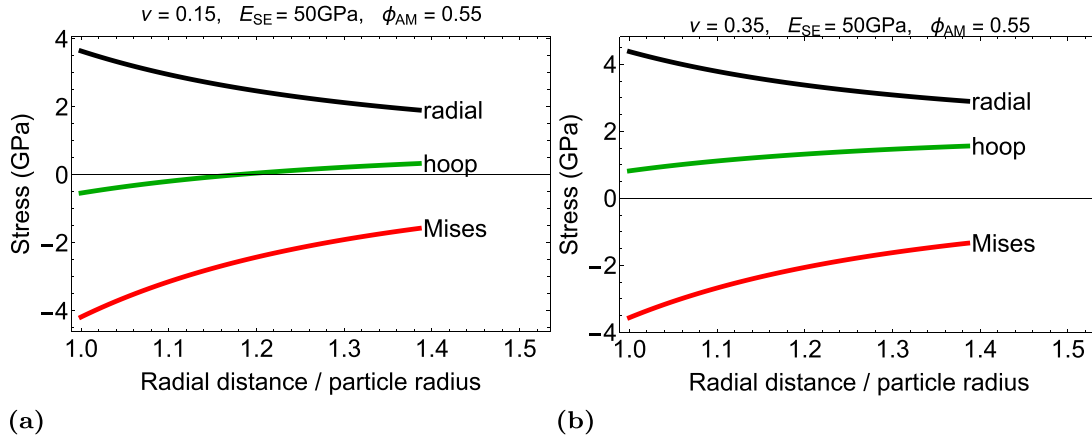
FIG. 6. A plot of stress fields in the solid-electrolyte shell as a function of Possion's ratio (a) $\nu = 0.15$ (b) $\nu = 0.35$. The stress fields are developed during the charging process, where the embedded electrode particle shrinks in size. E_{se} is the Young's modulus of solid electrolyte and ϕ_{AM} is the volume ratio of active material.

the delaminated surface of a spherical particle as a reflective boundary. Each of the 1000 random walkers, starting from the particle's center, moves in a succession of random steps until it escapes the particle.

The results of the analysis are presented in Figs. 8(a) and 8(b) and they are organized by the ratio of permeable (intact) vs not-permeable (delaminated) particle's surface. The data are normalized with respect to the values of mean and
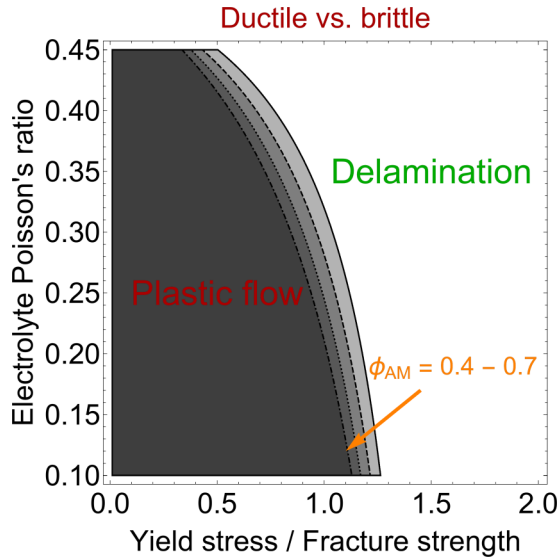

FIG. 7. If elastoplastic constitutive behavior is assumed for the solid electrolyte, the SE shell may undergo plastic flow in proximity to the interface. Depending on the electrolyte yield stress σ_{yield} and the interfacial fracture strength F_c, the system may release energy via plastic flow or fracture. The contour lines in Fig. 3(b) define the transition between these two modes according to Eq. (7). The result has a weak dependence on the volume fraction of active material, as highlighted by the shift of the contour lines. Such contour lines correspond, from right to left, to increasing volume ratios of active material (within the range 0.4–0.7). For any value of SE Poisson's ratio, plasticity will prevent fracture if the yield stress is not greater than half of the fracture strength.

standard deviation obtained for the intact particle (0% of delaminated boundary).

In the simulations the particle's surface is discretized with 2160 triangles. Two sets of analyses are carried out, by assuming the delaminated interface to be represented by contiguous or noncontiguous collections of discrete triangular elements [see Fig. 8(c)]. Discontinuous sets of fractured interfaces have been generated by randomly selecting discrete elements of the particle's surface. The random walk model tracks the trajectory of 1000 walkers moving from the center of a sphere. Each random step has a fixed length corresponding to 1% of the sphere's radius and a randomly generate orientation [see illustration on the top right of Fig. 8(c)]. The step is rejected if it intersects the delaminated region of the particle's surface (reflective boundary). The first passage time corresponds to the number of steps required to escape the particle through the undamaged surface.

The two cases are studied here to provide lower and upper bounds for the interface kinetics of partially delaminated particles. Unstable interfaces (i.e., in the "brittle" regime) will tend to propagate flaws catastrophically, leading to delaminated patches that are contiguous. On the other hand, stable interfaces (i.e., in the "ductile" regime) are tolerant of defects, and any delamination is more likely to remain locally contained. Realistic crack patterns are of course expected to be at least partially connected, but in general the surface kinetics of stable interfaces are expected to approach the behavior of the noncontiguous delamination model.

Yellow markers in Figs. 8(a) and 8(b) indicate the results for contiguous delaminated surfaces and show a relative increase of mean first passage time up to 2.75 and a fivefold increase in the standard deviation of FPTs. The effect of fracture is much less pronounced in the case of noncontiguous fracture surfaces [indicated by blue markers in Figs. 8(a) and 8(b)].

This result indicates that interfacial kinetics depends not only on the extension of the contact area but also on its connectivity. It is possible that engineering a rough, stable interface may result in discontinuous delamination patches and a low average resistance.
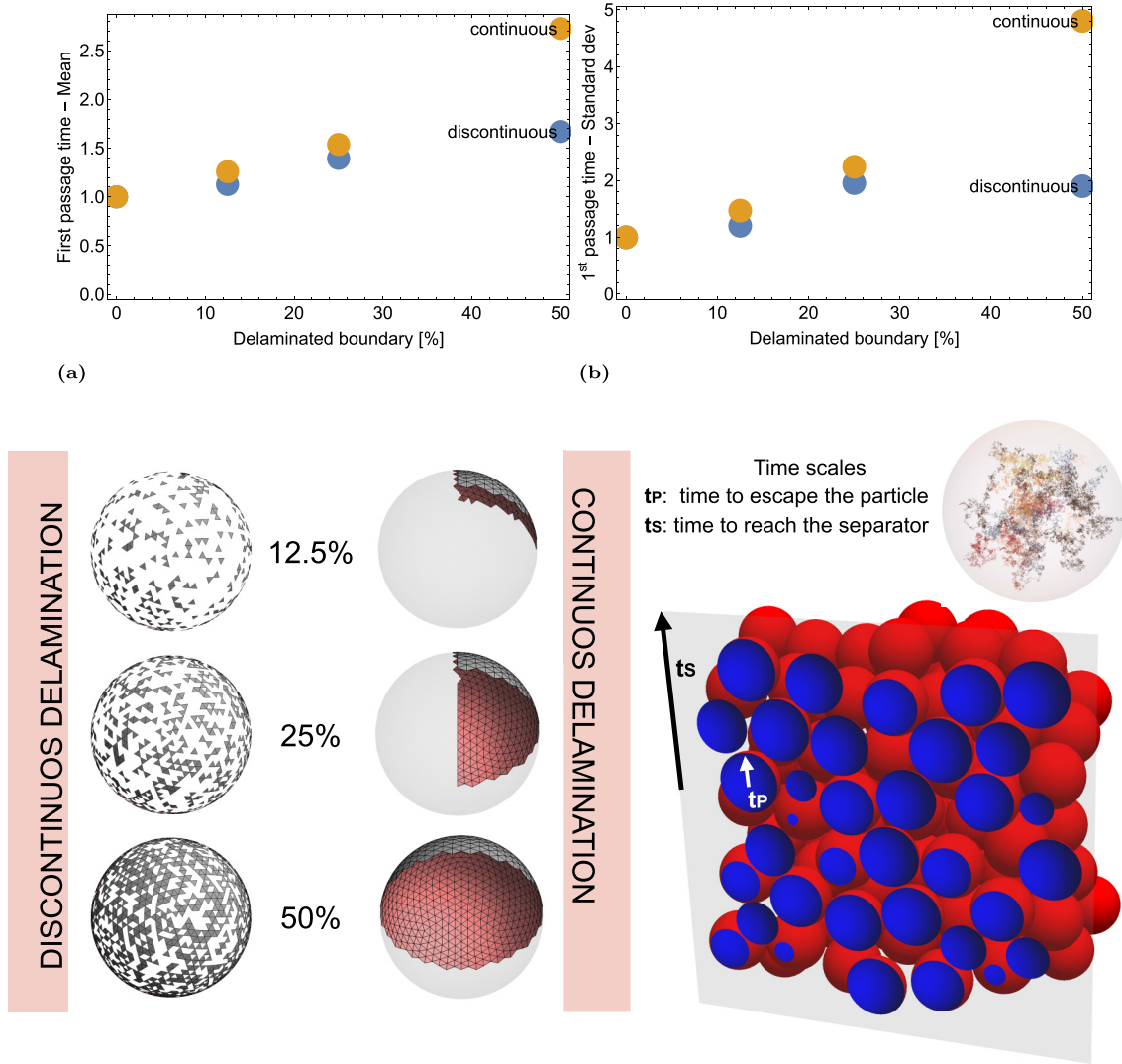
FIG. 8. Via random walk analysis we calculate the first passage from the center to the surface of a partially delaminated spherical particle. The delaminated surface is treated as a reflective boundary. The particle's surface is discretized with 2160 triangles and delaminated surfaces are either contiguous or noncontiguous collections of triangles [see panel (c)]. A large shift in both mean and standard deviation of the first passage times is observed when delaminated surfaces are contiguous [see panels (a) and (b)]. The average deintercalation (intercalation) time increases with delamination; however, the impact on the total charging (discharging) time may be small, if the particle radius is small compared to the electrode thickness or if the electrolyte is not very conductive.

During battery charge, the transport of Li within the positive electrode is characterized by two timescales: the time to deintercalate a particle t_P and the time to reach the separator t_S [see Fig. 8(c)]. The weight of each time scale depends on the electrode's geometry and the relative mobility of Li in the two media. For instance, if the particle's diameter is one tenth of the electrode thickness, but the mobility of Li is ten times faster in the electrolyte, the two timescales t_P and t_S are equal. In this case, a twofold increase of t_P, due to delamination, raises the total charge/discharge time by 150% (from $t_P + t_S = 2t_P$ to $3t_P$). For highly conductive electrolyte ($t_P \gg t_S$), particle interfacial kinetics becomes the rate limiting step in achieving fast charging. Conversely, particle delamination has low impact on the overall cell power, when combined with low conductivity electrolyte ($t_S \gg t_P$).

The large data scattering obtained with contiguously delaminated particles can be interpreted as a nonuniform dis-

tribution of Li across the electrode thickness. Large concentration and stress gradients may form in regions surrounding impenetrable interfaces.

III. CONCLUSIONS

For the elastic moduli, interfacial toughness, and expansion coefficients considered, our analysis of all-solid-state battery reliability indicates that positive electrode particles are likely to delaminate upon battery charging.

During battery charge lithium deintercalates from the positive electrode causing the active material to contract. For most combinations of electrolyte and interfacial properties, delamination initiates when particles have changed their radius by only 2.5% (and their volume by 7.5%), a value that encompasses the behavior of many intercalation compounds [21,22]. Systems with more compliant electrolytes and larger cohesive

energy are less amenable to delamination. For instance, in the case of electrolyte Young's modulus lower than 25 GPa and interfacial cohesive energy $\gamma_{am\text{-}se} > 5$ Jm^{-2}, delamination requires more than 25% of (intercalation-induced) volumetric strain.

Delamination occurs independently of the particle size, therefore nanostructured electrodes have no advantage in this case. Once fracture nucleates, whether the crack opening proceeds gradually ("ductile") or abruptly ("brittle") depends on the relative length scales and on the relative stiffness of bulk solid electrolyte material and interface.

For a given cohesive length and particle radius, stable crack growth is characterized by high SE stiffness and low interfacial fracture energy. A much wider range of SE materials can be used, in combination with nanostructured electrodes, with particles size in the order of 100 nm. For nanoparticles, delamination occurs but it proceeds smoothly and it may not reach completion. Mechanical stability is also promoted in densely packed microstructures characterized by a large damage zone ahead of the crack tip.

Furthermore, delamination is prevented if the solid-electrolyte plastically deforms and relaxes the stress at the electrode-electrolyte interface. The plastic deformation occurs if the yield stress of the solid electrolyte is lower than the interfacial cohesive strength, $\sigma_{\text{yield}} < 0.5F_c$. The Poisson's ratio and the volume fraction of electrode particles further affect the plastic flow of the electrolyte. The design criterion ($\sigma_{\text{yield}} < 0.5F_c$) provides a "rule of thumb" to engineer the interfacial cohesive strength (and/or eletrolyte yield stress) to prevent delamination.

As the contact area between particles and electrolyte decreases, the area-specific impedance increases. Our random walk analyses investigate the relationship between internal resistance and the extension and connectivity of delaminated interfaces. Stable interfaces can be expected to maintain distributed regions of contact at the particle's surface, a condition which is shown to preserve good rate performance over cycling. Furthermore, allowing the system to release energy and relax the stress by controlled fracturing could be an effective strategy to avoid further mechanical degradation.

There are two timescales associated with charging and discharging: a diffusion time associated with the composite electrode thickness and another associated with the particle radius. The longest timescale determines the charge/discharge capability. If highly conductive electrolytes are employed, the particle interfacial kinetics dominates the power density of the cell.

[1] K. Takada, Progress and prospective of solid-state lithium batteries, Acta Mater. **61**, 759 (2013).

[2] J. Li, C. Ma, M. Chi, C. Liang, and N. J. Dudney, Solid electrolyte: The key for high-voltage lithium batteries, Adv. Energy Mater. **5**, 1 (2015).

[3] J. G. Kim, B. Son, S. Mukherjee, N. Schuppert, A. Bates, O. Kwon, M. J. Choi, H. Y. Chung, and S. Park, A review of lithium and non-lithium based solid state batteries, J. Power Sources **282**, 299 (2015).

[4] V. Thangadurai, S. Narayanan, and D. Pinzaru, Garnet-type solid-state fast Li ion conductors for Li batteries: Critical review, Chem. Soc. Rev. **43**, 4714 (2014).

[5] J. Janek and W. G. Zeier, A solid future for battery development, Nat. Energy **1**, 16141(EP) (2016).

[6] Y. Kato, S. Hori, T. Saito, K. Suzuki, M. Hirayama, A. Mitsui, M. Yonemura, H. Iba, and R. Kanno, High-power all-solid-state batteries using sulfide superionic conductors, Nat. Energy **1**, 16030(EP) (2016).

[7] K. H. Kim, Y. Iriyama, K. Yamamoto, S. Kumazaki, T. Asaka, K. Tanabe, C. A. J. Fisher, T. Hirayama, R. Murugan, and Z. Ogumi, Characterization of the interface between LiCoO$_2$ and Li$_7$La$_3$Zr$_2$O$_{12}$ in an all-solid-state rechargeable lithium battery, J. Power Sources **196**, 764 (2011).

[8] T. Kobayashi, A. Yamada, and R. Kanno, Interfacial reactions at electrode/electrolyte boundary in all solid-state lithium battery using inorganic solid electrolyte, thio-LISICON, Electrochim. Acta **53**, 5045 (2008).

[9] E. Jeong, C. Hong, Y. Tak, S. C. Nam, and S. Cho, Investigation of interfacial resistance between LiCoO$_2$ cathode and LiPON electrolyte in the thin film battery, J. Power Sources **159**, 223 (2006), special issue, *3rd International Conference on Materials for Advanced Technologies (ICMAT-2005) and 9th International Conference on Advanced Materials (ICAM 2005)*, Singapore (2005).

[10] A. Sakuda, A. Hayashi, and M. Tatsumisago, Intefacial observation between LiCoO$_2$ electrode and Li$_2$S − P$_2$S$_5$ solid electrolytes of all-solid-state lithium secondary batteries using transmission electron microscopy, Chem. Mater. **22**, 949, (2010).

[11] K. K. Fu, Y. Gong, G. T. Hitz, D. W. McOwen, Y. Li, S. Xu, Y. Wen, L. Zhang, C. Wang, G. Pastel, J. Dai, B. Liu, H. Xie, Y. Yao, E. D. Wachsman, and L. Hu, Three-dimensional bilayer garnet solid electrolyte based high energy density lithium metal-sulfur batteries, Energy Environ. Sci. **10**, 1568 (2017).

[12] M. Nagao, A. Hayashi, and M. Tatsumisago, High-capacity Li$_2$S-nanocarbon composite electrode for all-solid-state rechargeable lithium batteries, J. Mater. Chem. **22**, 10015 (2012).

[13] M. Jak, M. Pontfoort, N. Van Landschoot, A. Best, E. Kelder, D. MacFarlane, M. Forsyth, and J. Schoonman, Composite cell components for elevated temperature all-solid-state Li-ion batteries, Solid State Ionics **143**, 57 (2001).

[14] P. Birke, F. Salam, S. Doring, and W. Weppner, A first approach to a monolithic all solid state inorganic lithium battery, Solid State Ionics **118**, 149 (1999).

[15] K. Chen, Y. Shen, Y. Zhang, Y. Lin, and C.-W. Nan, High capacity and cyclic performance in a three-dimensional composite electrode filled with inorganic solid electrolyte, J. Power Sources **249**, 306 (2014).

[16] S. Ohta, S. Komagata, J. Seki, T. Saeki, S. Morishita, and T. Asaoka, All-solid-state lithium ion battery using garnet-type oxide and Li_3BO_3 solid electrolytes fabricated by screen-printing, J. Power Sources **238**, 53 (2013).

[17] F. Rosciano, P. P. Pescarmona, K. Houthoofd, A. Persoons, P. Bottke, and M. Wilkening, Towards a lattice-matching solid-state battery: Synthesis of a new class of lithium-ion conductors with the spinel structure, Phys. Chem. Chem. Phys. **15**, 6107 (2013).

[18] A. Aboulaich, R. Bouchet, G. Delaizir, V. Seznec, L. Tortet, M. Morcrette, P. Rozier, J.-M. Tarascon, V. Viallet, and M. Dolle, A new approach to develop safe all-inorganic monolithic Li-ion batteries, Adv. Energy Mater. **1**, 179 (2011).

[19] G. Delaizir, V. Viallet, A. Aboulaich, R. Bouchet, L. Tortet, V. Seznec, M. Morcrette, J.-M. Tarascon, P. Rozier, and M. Dolle, The Stone Age revisited: Building a monolithic inorganic lithium-ion battery, Adv. Funct. Mater. **22**, 2140 (2012).

[20] R. Kanno, M. Murayama, T. Inada, T. Kobayashi, K. Sakamoto, N. Sonoyama, A. Yamada, and S. Kondo, A self-assembled breathing interface for all-solid-state ceramic lithium batteries, Electrochem. Solid State Lett. **7**, A455 (2004).

[21] W. H. Woodford, Electrochemical Shock: Mechanical Degradation of Ion-Intercalation Materials, Ph.D. thesis, Massachusetts Institute of Technology (2013).

[22] A. Mukhopadhyay and B. W. Sheldon, Deformation and stress in electrode materials for Li-ion batteries, Prog. Mater. Sci. **63**, 58 (2014).

[23] E. Peled, D. Golodnitsky, C. Menachem, and D. Bar-Tow, An advanced tool for the selection of electrolyte components for rechargeable lithium batteries, J. Electrochem. Soc. **145**, 3482 (1998).

[24] J. Li, E. Murphy, J. Winnick, and P. A. Kohl, The effects of pulse charging on cycling characteristics of commercial lithium-ion batteries, J. Power Sources **102**, 302 (2001).

[25] T. Zheng, A. S. Gozdz, and G. G. Amatucci, Reactivity of the solid electrolyte interface on carbon electrodes at elevated temperatures, J. Electrochem. Soc. **146**, 4014 (1999).

[26] G. Del Piero, *A Variational Approach to Fracture and Other Inelastic Phenomena* (Springer Netherlands, Dordrecht, 2014), pp. 3–77.

[27] A. Evans and J. Hutchinson, On the mechanics of delamination and spalling in compressed films, Int. J. Solids Struct. **20**, 455 (1984).

[28] D. Marshall and A. Evans, Measurement of adherence of residually stressed thin films by indentation. I. Mechanics of interface delamination, J. Appl. Phys. **56**, 2632 (1984).

[29] Y. Wei and J. Hutchinson, Nonlinear delamination mechanics for thin films, J. Mech. Phys. Solids **45**, 1137 (1997).

[30] A. Argon, V. Gupta, H. Landis, and J. Cornie, Intrinsic toughness of interfaces, Mater. Sci. Eng. A **107**, 41 (1989).

[31] A. Needleman, An analysis of decohesion along an imperfect interface, Int. J. Fract. **42**, 21 (1990).

[32] A. Needleman, Analyses of interfacial failure, Appl. Mech. Rev. **43**, S274 (1990).

[33] G. Del Piero and L. Truskinovsky, Macro- and micro-cracking in one-dimensional elasticity, Int. J. Solids Struct. **38**, 1135 (2001).

[34] N. H. MacMillan, The theoretical strength of solids, J. Mater. Sci. **7**, 239 (1972).

[35] T. Hong, J. R. Smith, and D. J. Srolovitz, Theory of metal-ceramic adhesion, Acta Metall. Mater. **43**, 2721 (1995).

[36] Y. Qi and L. G. Hector, Adhesion and adhesive transfer at aluminum/diamond interfaces: A first-principles study, Phys. Rev. B **69**, 235401 (2004).

[37] M. F. Ashby, *Materials Selection in Mechanical Design* (Elsevier, New York, 2011).